

Estimation of regional lung expansion via 3D image registration

Yan Pan¹, Dinesh Kumar¹, Eric A. Hoffman¹, Gary E. Christensen¹, Geoffrey McLennan¹,
Joo Hyun Song¹, Alan Ross¹, Brett A. Simon², and Joseph M. Reinhardt¹

¹Univ. of Iowa, Iowa City, IA

²Johns Hopkins Med. Inst., Baltimore, MD

ABSTRACT

A method is described to estimate regional lung expansion and related biomechanical parameters using multiple CT images of the lungs, acquired at different inflation levels. In this study, the lungs of two sheep were imaged utilizing a multi-detector row CT at different lung inflations in the prone and supine positions. Using the lung surfaces and the airway branch points for guidance, a 3D inverse consistent image registration procedure was used to match different lung volumes at each orientation. The registration was validated using a set of implanted metal markers. After registration, the Jacobian of the deformation field was computed to express regional expansion or contraction. The regional lung expansion at different pressures and different orientations are compared.

Keywords: Image registration, lung, biomechanics, X-ray CT

1. INTRODUCTION

There is great interest in studying the biomechanical properties of the lung since disease processes, such as emphysema and fibrosis, can alter the lung biomechanical characteristics and disrupt lung function. The use of pulmonary imaging technologies as non-invasive methods to study regional lung structure and function are particularly valuable because lung disease is heterogeneous and significant pathological tissue change may occur before it can be detected by traditional lung measurements.^{1,2}

Imaging can be used to study the biomechanical properties of lung tissue. Early work used implanted parenchymal markers to measure regional lung expansion.³⁻⁶ In [3-6], biplane X-ray imaging was used to determine the locations of the implanted markers. Using the marker locations at various lung inflation levels, regional lung behavior can be described. Using this technique, Hubmayr et al. examined the distribution of regional lung volume during deflation from TLC to FRC⁴ and during mechanical ventilation and spontaneous breathing in dogs.⁶ Rodarte et al⁵ studied regional lung tissue deformation and tissue strain using implanted markers, and compared the lung tissue strain in different lobes and in the supine and prone orientations. More recently, Hubmayr et al.⁷ investigated the regional lung expansion of constricted dogs using the parenchymal marker technique.

High resolution X-ray computed tomography (CT), which can acquire high spatial and temporal resolution volumetric pulmonary images within a breath hold, has been widely used for both clinical and research work. CT images provide detailed information regarding pulmonary structure and structure-function relationships.² Instead of studying aggregate structures or function, CT imaging can be used to measure regional lung volumes, regional expansion and other mechanical properties. Coxson et al.⁸ studied total and regional lung volumes using CT and compared these with quantitative histology, and they concluded that the measurement of the proportions of tissue and air within the thorax can be used to evaluate lung structure. Hoffman^{9,10} used a unique X-ray CT scanner, the Dynamic Spatial Reconstructor, to study in vivo lung geometry and function in prone and supine dogs and sloths. It was shown that a gradient of fractional lung air content in the ventral-dorsal

Send correspondence to J.M.R.: joe-reinhardt@uiowa.edu; phone 1 319 335 5634; fax 1 319 335 5632; 1402 SC, Univ. of Iowa, Iowa City, IA 52242

direction occurs in supine posture, and but that an approximately uniform air content distribution occurs in the prone posture. Olson and Hoffman¹¹ determined lung volumes, gradients in lung air content, and maximum in vivo lung dimensions in pneumonectomized rabbits in prone and supine orientations with an EBCT scanner. In another study,¹² fast dynamic computed tomography has been used to study ventilation induced changes in lung density distribution. Krishnan et al.¹³ studied regional lung ventilation by mapping lung regions at different lung volumes using a warping function determined by manually-selected landmarks. The method from [13] was used to compute the volume change, air content distribution, and mean density change during lung inflation.

Magnetic resonance (MR) imaging can also be used to quantitatively measure regional lung tissue density, pulmonary ventilation distribution, and regional lung function.^{14,15} Gee et al.¹⁶ registered successive serial MR images acquired during respiration, and modeled the deformation of the lung tissue as an elastic deformation. Local lung tissue deformation was quantified using the Lagrangian strain which was derived from the calculated motion fields.

This paper describes a method to study regional lung expansion by matching lung regions across lung volume changes through 3D registration. In this approach, multiple CT images of lung acquired at five different pressures are registered using anatomic landmarks and lung tissue intensities. The registration is validated by implanted metallic markers. The deformation field derived from the registration is used to compute regional expansion. The method is demonstrated using CT images of two animals with image data acquired in the prone and supine orientations.

2. MATERIALS AND METHODS

2.1. Volumetric CT Imaging Data Acquisition

All animal studies were performed using a protocol approved by the University of Iowa Animal Care and Use Committee. Two sheep were used in this study. Metallic markers (0.055 inch in diameter) were surgically implanted in the lungs of two anesthetized sheep through a sternotomy procedure. Sixty-seven markers were implanted in sheep 1; 103 markers were implanted in sheep 2. For both animals the markers were implanted mainly in the left upper lobe and right lower lobe.

Approximately six weeks after marker implantation, volumetric CT images of the thorax were acquired in the prone and supine body orientations at five different airway pressures: 0, 8, 16, 24, and 32 cm H₂O. Images were acquired for each airway pressure using a multi-detector row CT scanner (model MX8000 Quad Scanner; Philips, The Netherlands). The slice thickness was 1.3 mm and slice spacing was 0.6 mm. The reconstruction matrix was 512 × 512 pixels. In-plane pixel size was approximately 0.47 × 0.47 mm² for sheep 1 and 0.49 × 0.49mm² for sheep 2.

2.2. Image Preprocessing and Preparation for Registration

Before matching lung regions across different lung volumes by 3D registration, a sequence of preprocessing steps is applied. Figure 1 shows a flow chart of the preprocessing steps.

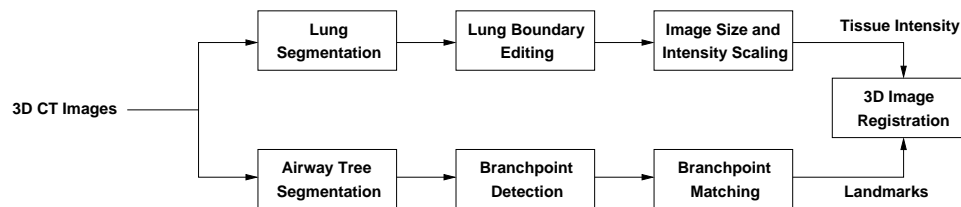


Figure 1. Flow chart showing the image preprocessing steps.

2.2.1. Image Segmentation

The lung segmentation method from [17] is applied to identify the lung boundary. In order to obtain a smooth boundary and consistent segmentation results across images acquired at different pressures, the results of the automatic segmentation were edited as needed.

The airway tree segmentation and analysis are based on the method from [18]. The airway tree is segmented using an iterative region-grow algorithm and skeletonized using a sequential thinning algorithm. The resulting skeleton is guaranteed to follow the center of the airways, and the branchpoints are positioned at their anatomically correct locations (Figure 2). The skeletonized tree is converted into a mathematical graph representation, which is subsequently used for branchpoint matching between different trees.

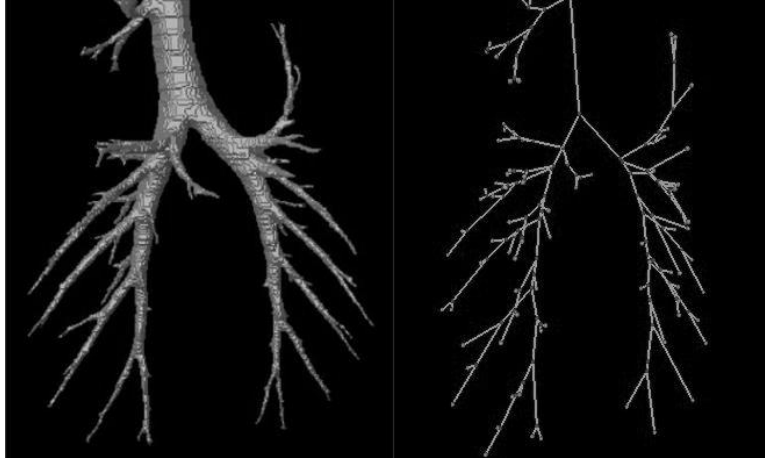


Figure 2. Airway tree analyses: (left) the segmented airway tree; (right) the skeletonized airway tree with airway branchpoints marked.

2.2.2. Preparation for Image Registration

To reduce memory requirements during the image registration, we convert the original 16-bit CT data to 8-bit values using a window of $[-1000\text{HU}, -400\text{HU}]$. The image data is downsampled by a factor of two, and padded to give dimensions that are a power of two. After downsampling and padding, the data sets are of size $256 \times 256 \times 256$ voxels.

2.3. Consistent Landmark and Intensity-based Registration

The internal structure of the lung varies with lung expansion. In order to estimate the deformation of internal lung tissue, a 3D registration algorithm is used to define correspondences between images with different airway pressures. In this study, we use the consistent landmark and intensity registration algorithm described in [19, 20]. By matching corresponding landmarks and matching intensity away from landmarks, the algorithm produces good correspondences between the images in all the locations, while landmark-only methods may not get satisfactory registration results in locations far from the registration landmarks. In addition, compared to unidirectional algorithms, consistent registration algorithms jointly estimate the forward and reverse transformation between two images while minimizing the inverse consistency error.^{19, 20}

The registration method^{19, 20} jointly estimates the forward transformation from template image $T^{(i)}$ to target image $T^{(j)}$ and the reverse transformation from target to template image. The transformations are selected to

minimize a cost function given by

$$\begin{aligned}
C = & \sigma \int_{\Omega} |T^{(i)}(h^{(i,j)}(x)) - T^{(j)}(x)|^2 + |T^{(j)}(h^{(j,i)}(x)) - T^{(i)}(x)|^2 dx + \\
& \rho \int_{\Omega} \|Lu^{(i,j)}(x)\|^2 + \|Lu^{(j,i)}(x)\|^2 dx + \\
& \chi \int_{\Omega} \|u^{(i,j)}(x) - \tilde{u}^{(j,i)}(x)\|^2 + \|u^{(j,i)}(x) - \tilde{u}^{(i,j)}(x)\|^2 dx,
\end{aligned} \tag{1}$$

where Ω is the domain of the image, the mapping $h^{(i,j)}$ is defined as the transformation that warps the template image into the shape of the target image, and $h^{(j,i)}$ is the reverse transformation. $u^{(i,j)}(x) = x - h^{(i,j)}(x)$, for $x \in \Omega$, represents the displacement field from the template image to the target image, $u^{(j,i)}(x) = x - h^{(j,i)}(x)$ represents the reverse displacement field. The first integral in the cost function defines the cumulative squared error similarity cost between the deformed template image $T^{(i)}(h^{(i,j)}(x))$ and the target image and between the deformed target image $T^{(j)}(h^{(j,i)}(x))$ and the template image. This term minimizes the squared error intensity between the images. The second integral is used to regularize the forward and reverse displacement fields to meet the properties of linear elasticity and so that topological constraints are enforced on the transformation. The linear differential operator L as follows corresponds to the linear-elastic constraint,

$$Lu(x) = \alpha \nabla u(x) + \beta \nabla (\nabla \cdot u(x)) + \gamma u(x) \tag{2}$$

where $\nabla^2 = (\partial^2/\partial x^2 + \partial^2/\partial y^2 + \partial^2/\partial z^2)$, and $\nabla(\nabla) = (\partial/\partial x + \partial/\partial y + \partial/\partial z) \cdot (\partial/\partial x + \partial/\partial y + \partial/\partial z)$. α, β, γ are constants associated with the linear-elastic constitutive law. The third integral in (1) is the inverse consistency constraint. The inverse consistency constraint is minimized when the forward transformation is the inverse of the reverse transformation. The inverse consistency constraint ensures that the mapping from template to target is the reverse of the mapping from target to template, in other words, it is a one-to-one mapping. The parameters σ, ρ, χ are the weights for each part of the cost function. In this study, $\sigma = 1, \rho = 0.00125, \chi = 600$ was used.

Registration was performed on four resolution levels (0.0625, 0.125, 0.25, and 0.5 of full size). At each resolution level a maximum of 20 iterations was allowed. The airway branch points detected using method described in Section 2.2.1 were used as registration landmarks. After airway tree segmentation, branch points were chosen and manually matched for each pair of volume datasets (0–8, 8–16, 16–24, and 24–32 cm H₂O). During registration the similarity cost, linear elasticity cost, inverse consistency cost, total cost, and registration landmark cost are plotted to assess algorithm performance.

2.4. Registration Validation

The registration performance was evaluated through three indexes: (1) the landmark error, defined as the registration error at the registration landmarks; (2) the marker error, defined as the error between the actual marker location and the marker location predicted by the image registration; and (3) the volume overlap error. The volume overlap error is a measurement of the overlap of the deformed template image and the target image:

$$\text{volume overlap error} = 1 - \frac{|I_{deformed} \cap I_{target}|}{|I_{deformed} \cup I_{target}|} \tag{3}$$

where $I_{deformed}$ and I_{target} are the sets of voxels that make up the deformed and target images and $|\cdot|$ represents area.

2.5. Regional Lung Expansion

Regional lung expansion was evaluated by examining the deformation functions computed during image registration. Consider the lung deformation function $u(x, y, z)$. The Jacobian $J(x, y, z)$ of the transformation

$u(x, y, z)$ is

$$J(x, y, z) = \begin{vmatrix} \frac{\partial u_x(x,y,z)}{\partial x} & \frac{\partial u_x(x,y,z)}{\partial y} & \frac{\partial u_x(x,y,z)}{\partial z} \\ \frac{\partial u_y(x,y,z)}{\partial x} & \frac{\partial u_y(x,y,z)}{\partial y} & \frac{\partial u_y(x,y,z)}{\partial z} \\ \frac{\partial u_z(x,y,z)}{\partial x} & \frac{\partial u_z(x,y,z)}{\partial y} & \frac{\partial u_z(x,y,z)}{\partial z} \end{vmatrix}.$$

The Jacobian measures the differential expansion at position (x, y, z) in the image. If the Jacobian is unity, there is no expansion or contraction. If the Jacobian is greater than one, there is local tissue expansion; if the Jacobian is less than one, there is local tissue contraction. To linearize the expansion measurement obtained via the Jacobian, it is sometimes useful to compare the logarithms of the regional Jacobian rather than the Jacobian itself.

3. RESULTS

3.1. 3D Image Registration

The landmark error, marker error, and overlap error were calculated to evaluate the registration. Since there are two sheep being studied, each examined in two orientations (prone and supine) and at five pressures, there are a total of 16 registration pairs. These pairs and the associated registration errors are presented in Table 1 and Figure 3. The mean landmark error is 1.11 mm, the maximum landmark error is 1.86 mm, the mean marker error is 1.38 mm, the maximum marker error is 2.58 mm, the mean volume overlap error is 0.04, and the maximum overlap error is 0.05.

Registration Pair	Study	Orientation	Registration Pair (cm H ₂ O)	Landmark error (mm)	Marker error (mm)	Overlap error
1	sheep 1	Supine	0 to 8	1.86	2.58	0.04
2	sheep 1	Supine	8 to 16	1.34	1.58	0.03
3	sheep 1	Supine	16 to 24	0.76	0.64	0.04
4	sheep 1	Supine	24 to 32	0.87	1.00	0.04
5	sheep 1	Prone	0 to 8	1.31	3.40	0.05
6	sheep 1	Prone	8 to 16	1.26	1.44	0.04
7	sheep 1	Prone	16 to 24	0.70	0.64	0.04
8	sheep 1	Prone	24 to 32	0.75	0.58	0.04
9	sheep 2	Supine	0 to 8	1.64	2.38	0.05
10	sheep 2	Supine	8 to 16	1.74	1.89	0.05
11	sheep 2	Supine	16 to 24	1.10	1.16	0.04
12	sheep 2	Supine	24 to 32	1.06	1.34	0.04
13	sheep 2	Prone	0 to 8	1.41	1.54	0.04
14	sheep 2	Prone	8 to 16	0.76	1.01	0.04
15	sheep 2	Prone	16 to 24	0.64	0.40	0.04
16	sheep 2	Prone	24 to 32	0.55	0.44	0.04

Table 1. Registration Validation: Landmark error, marker error, and overlap error for 16 pairwise registrations.

Figure 4 shows the template image, deformed template, and target image (sheep 1, prone, 0 cm H₂O–8 cm H₂O registration pair) to qualitatively illustrate the performance of the registration. The grid pictured on the right side is a unit grid deformed by the registration displacement field. This deformed grid shows that the displacement field is smooth and continuous.

The registration was also evaluated by examining the registration costs that make up equation 1. Figure 5 shows registration cost plots for sheep 2, prone orientation, 24 cm H₂O–32 cm H₂O at resolution 0.5. The figure shows that similarity cost and total cost decreases as the number of registration iteration increases, while the linear elasticity cost increases as the number of iterations increases. However, the landmark error and inverse consistency cost increase and decrease during registration processing because at each resolution level,

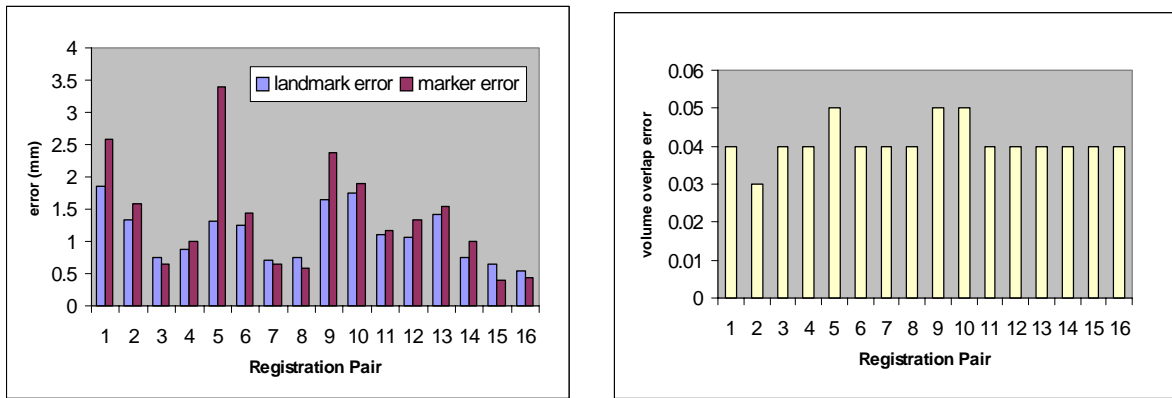


Figure 3. Graph of the landmark error, marker error and overlap error for the 16 registration pairs listed in Table 1.

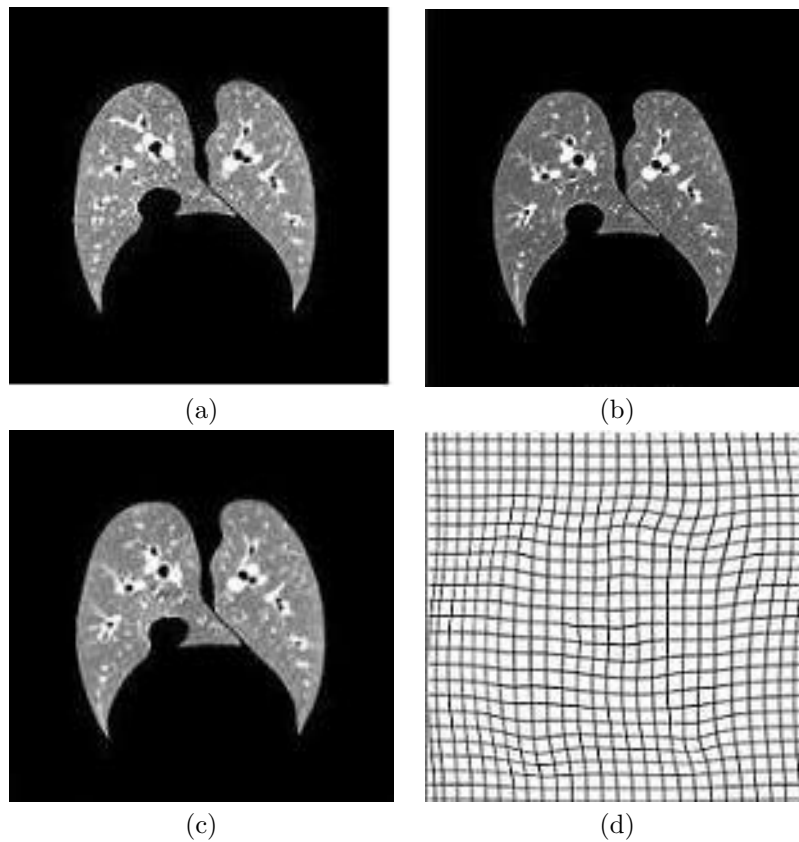


Figure 4. An example of one transverse slice from the template, target, deformed template images. (a) template image: sheep 1, prone orientation, 0 cm H₂O pressure; (b) target image: sheep 1, prone orientation, 8 cm H₂O pressure; (c) deformed template image after applying displacement field to match to the target image; (d) unit grid deformed by the registration displacement field.

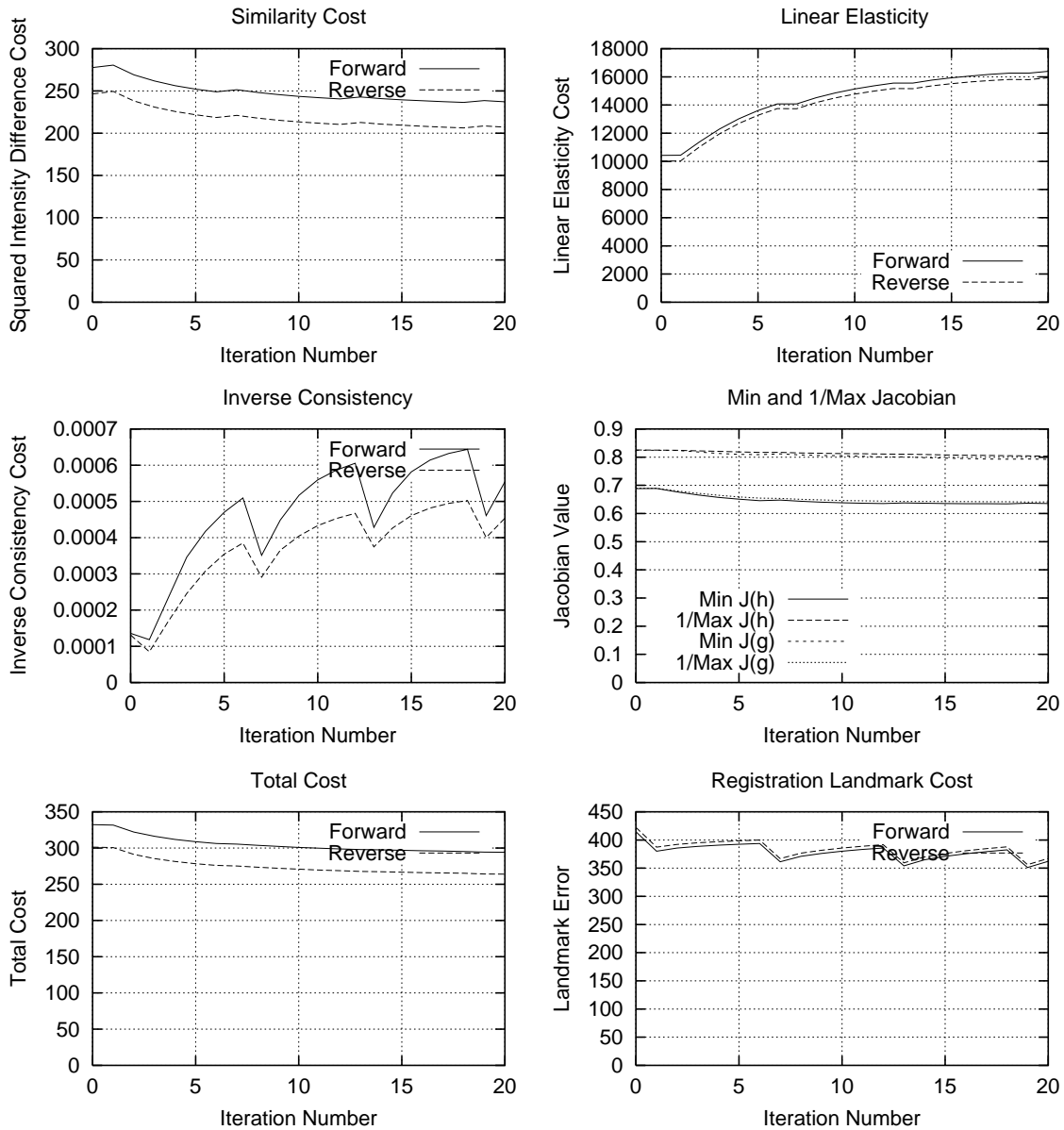


Figure 5. Registration Performance. The six plots show the similarity cost, linear elasticity, inverse consistency, maximum and minimum Jacobian value, total registration cost, landmark cost respectively as a function of registration iteration number.

the landmark based registration and intensity based registration are alternately performed. When the landmark registration is being performed, the inverse consistency cost may increase and during intensity registration, the landmark error may increase.

3.2. Regional lung expansion

Figure 6 shows the color-coded tranverse slice images of the log Jacobian of the registration displacement field for four pressure pairs (0–8, 8–16, 16–24, 24–32 cm H₂O) for the supine and prone orientations of sheep 1 and sheep 2. Figure 7 shows the log Jacobian image viewed from the transverse, sagittal, and coronal sections, for

the 8–16 cm H₂O pressure change pair for each sheep, each orientation. Figure 8 shows the mean Jacobian, averaged across all pixels on a coronal slice, plotted versus position from the non-dependent surface of the lung for each sheep and each orientation.

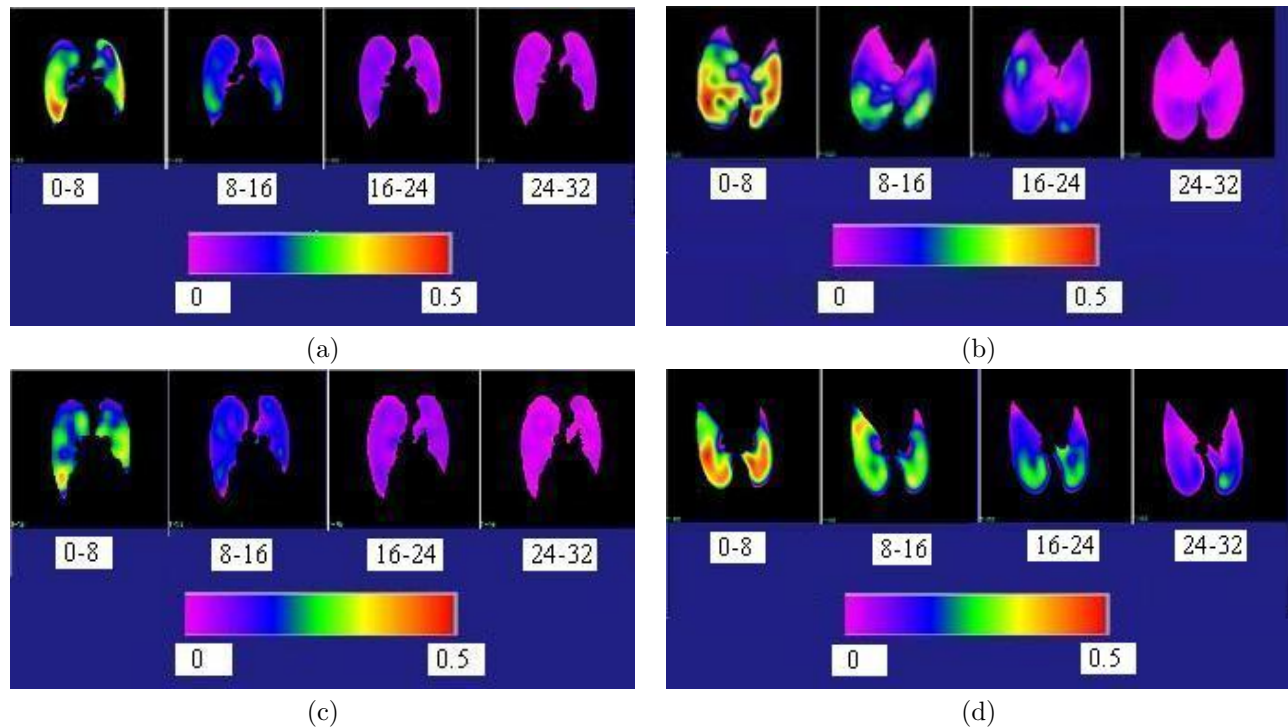


Figure 6. The log Jacobian image for a transverse slice for four pressure pairs. (a) sheep 1, prone orientation; (b) sheep 1, supine orientation; (c) sheep 2, prone orientation; (d) sheep 2, supine orientation.

4. DISCUSSION

All 16 pairwise registrations were judged satisfactory based on the landmark error, marker error, overlap error, displacement field, and the registration cost information. The image registration procedure was guided by tissue intensity and the airway branch points (landmarks). The number of landmarks affects the registration accuracy and computation time. It is not necessarily the case that adding additional landmarks will improve accuracy. In the regions close to the landmarks, the registration matches corresponding landmarks and interpolates between the landmark points. In regions away from registration landmarks, the tissue is matched using intensity information. If there are too many landmarks, the intensity information may not be fully used and registration accuracy away from the landmarks may suffer. Additionally, adding additional landmarks increases processing time.

While the bulk of lung segmentation processing is automatic, some manual intervention is occasionally needed. As an example, Figure 9 shows an automatic segmentation result that required manual editing. Since the registration processing depends on region intensity and boundary information, it was necessary to manually edit several data sets to force the segmentations to be consistent across all lung volumes and all body orientations.

The color-coded log Jacobian images (Figure 6) show that both in supine and prone orientations, the Jacobian values are greater over the lower pressure ranges than the higher ranges. These results confirm known physiology that the lung is more compliant at lower volumes than at higher volumes. These images (Figures 6 and 7) also demonstrate the greater homogeneity of lung expansion in the prone orientation.

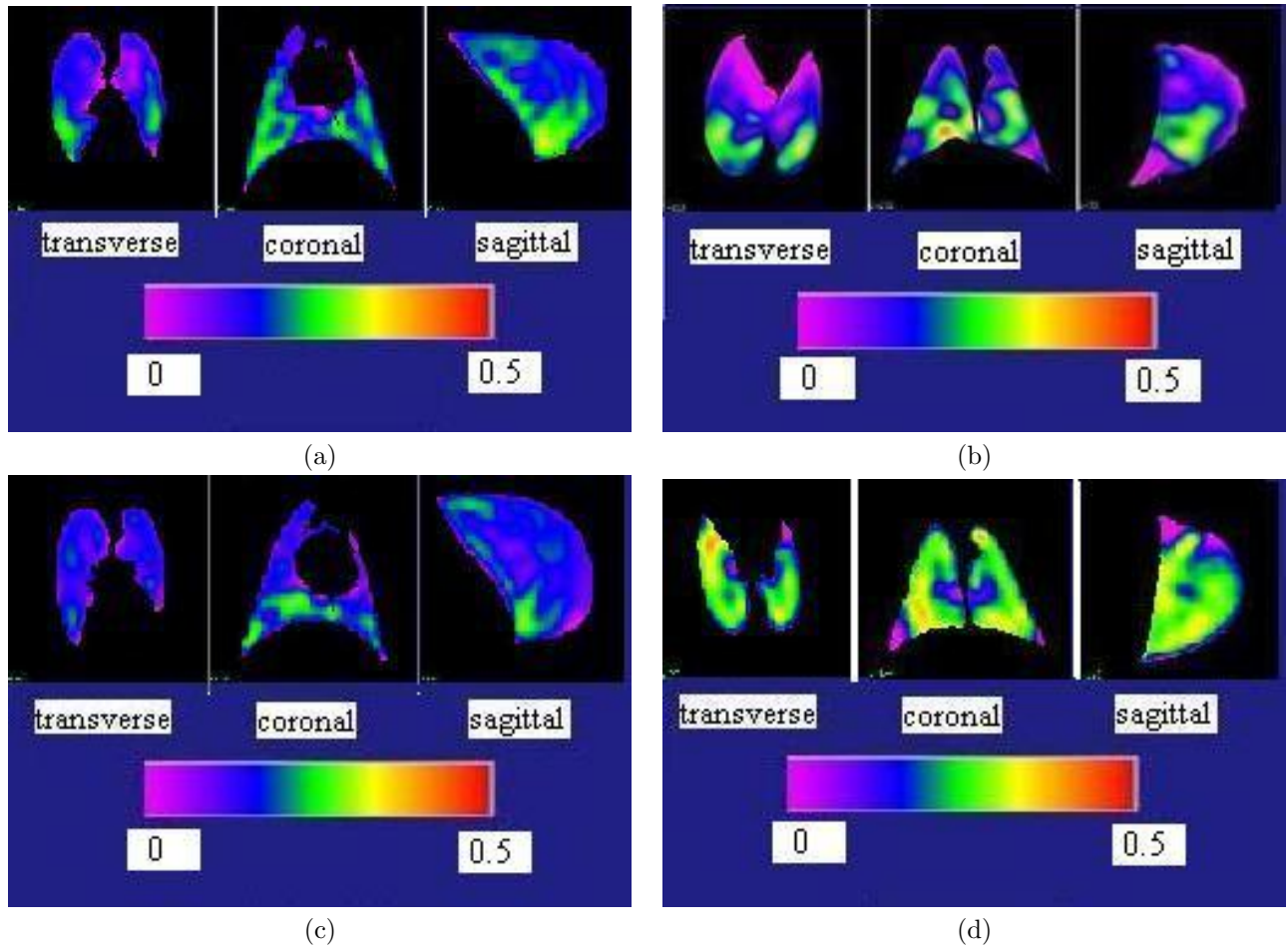


Figure 7. The log Jacobian image viewed from the transverse, sagittal, and coronal sections, for the 8–16 cm H₂O pressure change pair. (a) sheep 1, prone orientation; (b) sheep 1, supine orientation; (c) sheep 2, prone orientation; (d) sheep 2, supine orientation.

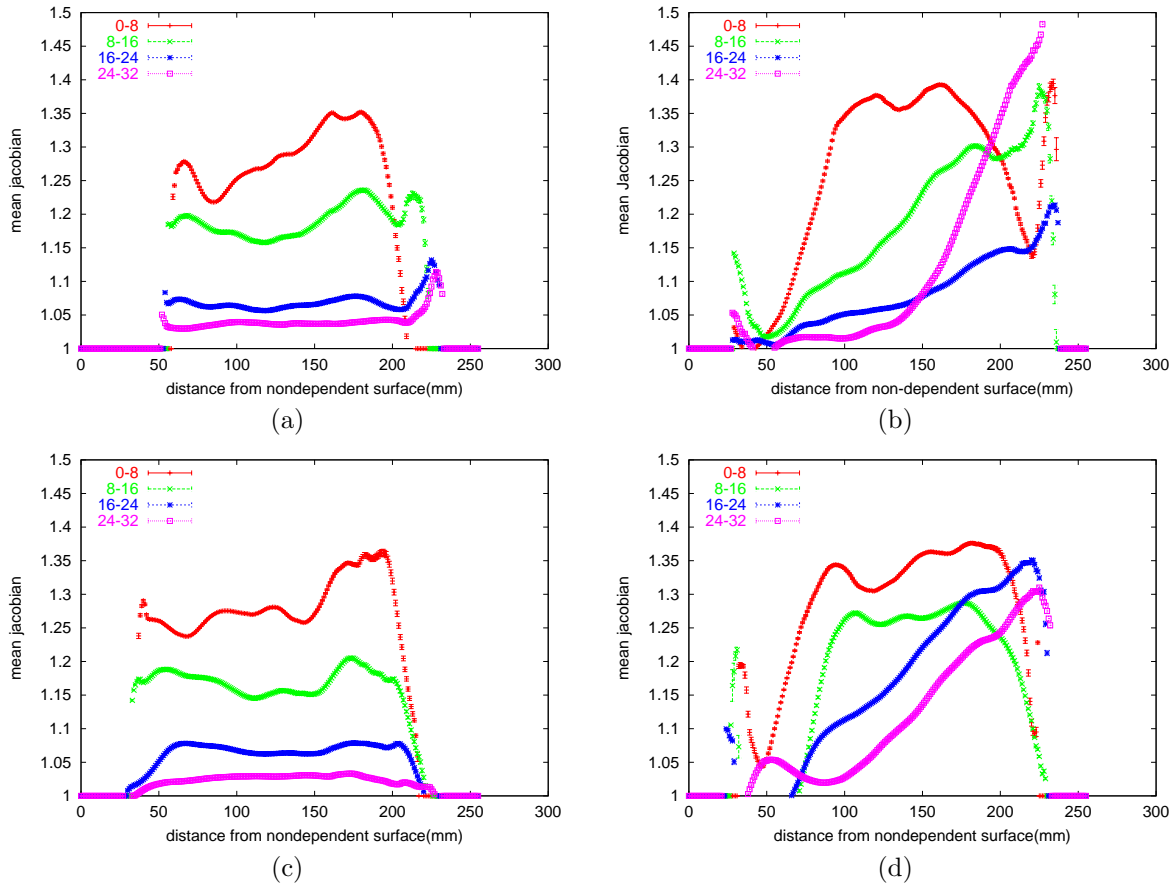


Figure 8. Mean Jacobian plots averaged across all pixels on a coronal slice, plotted versus position from the non-dependent surface. (a) sheep 1, prone orientation; (b) sheep 1, supine orientation; (c) sheep 2, prone orientation; (d) sheep 2, supine orientation.

The mean Jacobian plots (Figure 8) show that the expansion has a vertical gradient in the supine orientation while the prone vertical distribution of regional lung expansion is more uniform. Furthermore, in the supine position the gradient in the gravitational direction diminished as lung volume increased and shifter towards more dependent regions, reflecting the changing distribution of incremental volume changes as non-dependent regions become fully expanded and less compliant at lower airway pressures.

5. CONCLUSIONS

We have developed a procedure for calculating regional lung tissue expansion using image registration of multiple pressure-gated CT images. The results show that there are higher levels of regional lung expansion at the lower pressure steps (i.e., the start of inspiration) than at the higher pressure steps, consistent with the notion that the pressure volume curve is sigmoidal with the lung reaching non-compliant limits at higher inflation steps, and reaching these limits in the non-dependent regions of the supine lung at lower pressure steps. While these data are confirmatory of data obtainable from other methods, the technique now allows one to demonstrate the direction of principal strains, the x, y and z components of strain, regional ventilation in details unachievable by other methods (without introduction of tracer gases). By tracking identical lung regions, one is able to begin to answer important questions in clinical medicine such as “What is the regional lung response to a given ventilator regime?”

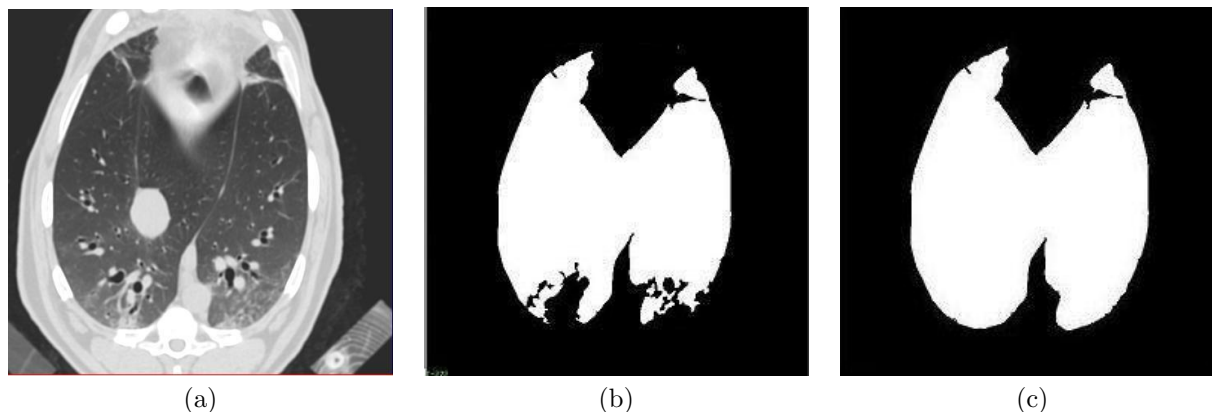


Figure 9. Manual editing of the initial lung segmentation mask was sometime necessary to get a consistent segmentation at all body orientations and pressures. (a) original lung image; (b) mask obtained by automatically segmenting lung; (c) refined lung mask after editing.

ACKNOWLEDGMENTS

The authors wish to thank Mr. Eric Peterson for performing the validation marker detection. This work was supported in part by grant HL64368 from the National Institutes of Health and by grant 0092758 from the National Science Foundation.

REFERENCES

1. B. A. Simon, "Non-invasive imaging of regional lung function using X-ray computed tomography," *J Clin Monit*, pp. 433–442, 2000.
2. E. A. Hoffman and G. McLennan, "Assessment of the pulmonary structure–function relationship and clinical outcomes measures: Quantitative volumetric CT of the lung," *Acad. Radiol.* **4**(11), pp. 758–776, 1997.
3. P. A. Chevalier, J. F. Greenleaf, R. A. Robb, and E. H. Wood, "Biplane videoroentgenographic analysis of dynamic regional lung strains in dogs," *J. Applied Physiology* **40**, pp. 118–122, Jan. 1976.
4. R. Hubmayr, B. Walters, P. Chevalier, J. Rodarte, and L. Olson, "Topographical distribution of regional lung volume in anesthetized dogs," *J. Applied Physiology* **54**(4), pp. 1048–1056, 1983.
5. J. R. Rodarte, R. D. Hubmayr, D. Stamenovic, and B. J. Walters, "Regional lung strain in dogs during deflation from total lung capacity," *J. Applied Physiology* **58**, pp. 164–172, Jan. 1985.
6. R. D. Hubmayr, J. R. Rodarte, B. J. Walters, and F. M. Tonelli, "Regional ventilation during spontaneous breathing and mechanical ventilation in dogs," *J. Applied Physiology* **63**, pp. 2467–2475, Dec 1987.
7. R. D. Hubmayr, M. J. Hill, and T. A. Wilson, "Nonuniform expansion of constricted dog lungs," *J. Applied Physiology* **80**(2), pp. 522–530, 1996.
8. H. O. Coxson, J. R. Mayo, H. Behzad, B. J. Moore, L. M. Verburgt, C. A. Staples, P. D. Paré, and J. C. Hogg, "Measurement of lung expansion with computed tomography and comparison with quantitative histology," *J Appl Physiol* **79**, pp. 1525–1530, Nov 1995.
9. E. A. Hoffman, "Effect of body orientation on regional lung expansion: A computed tomographic approach," *J. Applied Physiology* **59**(2), pp. 468–480, 1985.
10. E. A. Hoffman and E. L. Ritman, "Effect of body orientation on regional lung expansion in dog and sloth," *J. Applied Physiology* **59**(2), pp. 481–491, 1985.
11. L. E. Olson and E. A. Hoffman, "Lung volumes and distribution of regional air content determined by cine X-ray of pneumonectomized rabbits," *J. Applied Physiology* **76**(4), pp. 1774–1785, 1994.
12. K. Markstaller, H.-U. Kauczor, N. Weiler, J. Karmrodt, M. Doebrich, M. Ferrante, M. Thelen, and B. Eberle, "Lung density distribution in dynamic CT correlates with oxygenation in ventilated pigs with large ARDS," *British J. of Anaesthesia* **91**(5), pp. 699–708, 2003.

13. S. Krishnan, K. C. Beck, J. M. Reinhardt, K. A. Carlson, B. A. Simon, R. K. Albert, and E. A. Hoffman, "Regional lung ventilation from volumetric CT scans using image warping functions," *International Symposium on Biomedical Imaging*, 2004.
14. K. Ruppert, J. F. Mata, J. R. Brookeman, K. Hagspiel, and J. P. Mugler, "Detecting lung tissue density variations with XTC MRI," in *Scientific Meeting of the International Society of Magnetic Resonance in Medicine (I.S.M.R.M.)*, (Hawaii), May 2002.
15. B. T. Chen, A. C. Brau, and G. A. Johnson, "Measurement of regional lung function in rats using hyperpolarized $^3\text{helium}$ dynamic MRI," *Magnetic Resonance in Medicine* **49**, pp. 78–88, 2003.
16. J. Gee, T. Sundaram, I. Haseqawa, H. Uematsu, and H. Hatabu, "Characterization of regional pulmonary mechanics from serial magnetic resonance imaging data," *Acad. Radiol.* **10**, pp. 1147–1152, Oct 2003.
17. L. Shi, E. A. Hoffman, and J. M. Reinhardt, "Segmentation of the ovine lung in 3D CT images," in *Proc. SPIE Conf. Medical Imaging*, (San Diego, CA), 2004.
18. J. Tschirren, *Segmentation, Anatomical Labeling, Branchpoint Matching, and Quantitative Analysis of Human Airway Trees in Volumetric CT Images*. PhD thesis, The University of Iowa, 2003.
19. G. E. Christensen and H. J. Johnson, "Consistent image registration," *IEEE Transactions on Medical Imaging* **20**(7), pp. 568–582, 2001.
20. H. J. Johnson and G. E. Christensen, "Consistent landmark and intensity-based image registration," *IEEE Transactions on Medical Imaging* **21**(5), pp. 450–461, 2002.